Molecular Fingerprinting of Mouse Brain Using Ultrabroadband Coherent Anti-Stokes Raman Scattering (CARS) Microspectroscopy Empowered by Multivariate Curve Resolution-Alternating Least Squares (MCR-ALS)

Published as part of Chemical & Biomedical Imaging virtual special issue "Sub-diffraction Chemical Imaging".

Yusuke Murakami, Masahiro Ando, Ayako Imamura, Ryosuke Oketani, Philippe Leproux, Sakiko Honjoh, and Hideaki Kano*

Cite This: *Chem. Biomed. Imaging* 2024, 2, 689−697

Read Online

ACCESS | Metrics & More | Article Recommendations | SI Supporting Information

ABSTRACT: The Raman fingerprint spectral region provides abundant structural information on molecules. However, analyzing vibrational images within this region using coherent Raman imaging remains challenging due to the small Raman cross section and congested spectral features. In this study, we combined ultrabroadband coherent anti-Stokes Raman scattering (CARS) microspectroscopy across the spectral range of 500−4000 cm^{-1} with multivariate curve resolution-alternating least-squares (MCR-ALS) to reveal hidden Raman bands in the fingerprint region. Applying this method to mouse brain tissue, we extracted information on cholesterol and collagen, leveraging their distinctive molecular signatures, as well as on key molecules such as lipids, proteins, water, and nucleic acids. Moreover, the simultaneous detection of second harmonic generation facilitated label-free visualization of organelles, including arachnoid membrane and Rootletin filaments.

KEYWORDS: *molecular fingerprinting, coherent anti-Stokes Raman scattering, CARS, microscopy, multivariate curve resolution-alternating least-squares, MCR-ALS, brain*
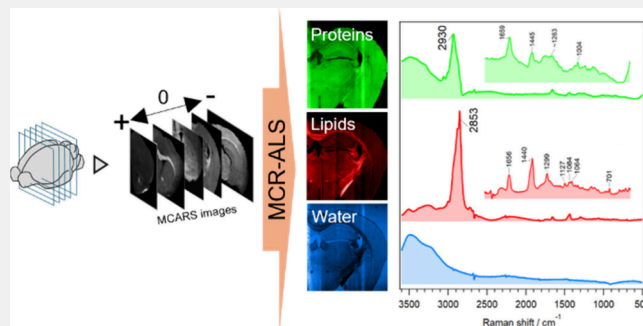
■ INTRODUCTION

Molecular imaging has been shown to be a valuable approach for understanding the functions of living cells and tissues through visualization of the distributions of biomolecules. Among molecular imaging techniques, fluorescence imaging, with dyes or proteins as labels, is commonly utilized. However, this approach has the disadvantage of the target molecule being perturbed by the exogenous bulky probe. By contrast, Raman spectroscopic imaging techniques are emerging as promising alternative approaches for molecular imaging. Among these, coherent Raman scattering (CRS) microscopy techniques, such as coherent anti-Stokes Raman scattering (CARS) and stimulated Raman scattering (SRS), are becoming increasingly accepted as indispensable tools that do not require the use of exogeneous labels or tags to decipher the complex molecular composition of biological systems.[1−11]

Historically, CRS microscopy has been primarily focused on the C−H stretching vibrational modes at Raman shifts of 2800−3100 cm^{-1}, which offer insights mainly into proteins and lipids. The range of Raman shifts typically detected in such imaging measurements is limited by the bandwidth of the laser source, which is approximately 200−300 cm^{-1}. The spectral coverage can be broadened by harnessing state-of-the-art laser sources,[6,12,13] such as a supercontinuum (SC) light source, allowing ultrabroadband CARS spectroscopic imaging to be realized. Using an SC light source, signals spanning the Raman shift range from 500 to 4000 cm^{-1}, which includes all the fundamental vibrational modes, can be collected.[14−20] This approach represents a breakthrough because it enables the extraction of detailed molecular information encoded in fingerprint CARS spectra. Based on such molecular fingerprint detection, various metabolites have been identified, such as squalene,[21] polysulfides,[22] dipicolic acid (DPA), and precursor molecules of DPA[23] using ultrabroadband CARS spectroscopic imaging.
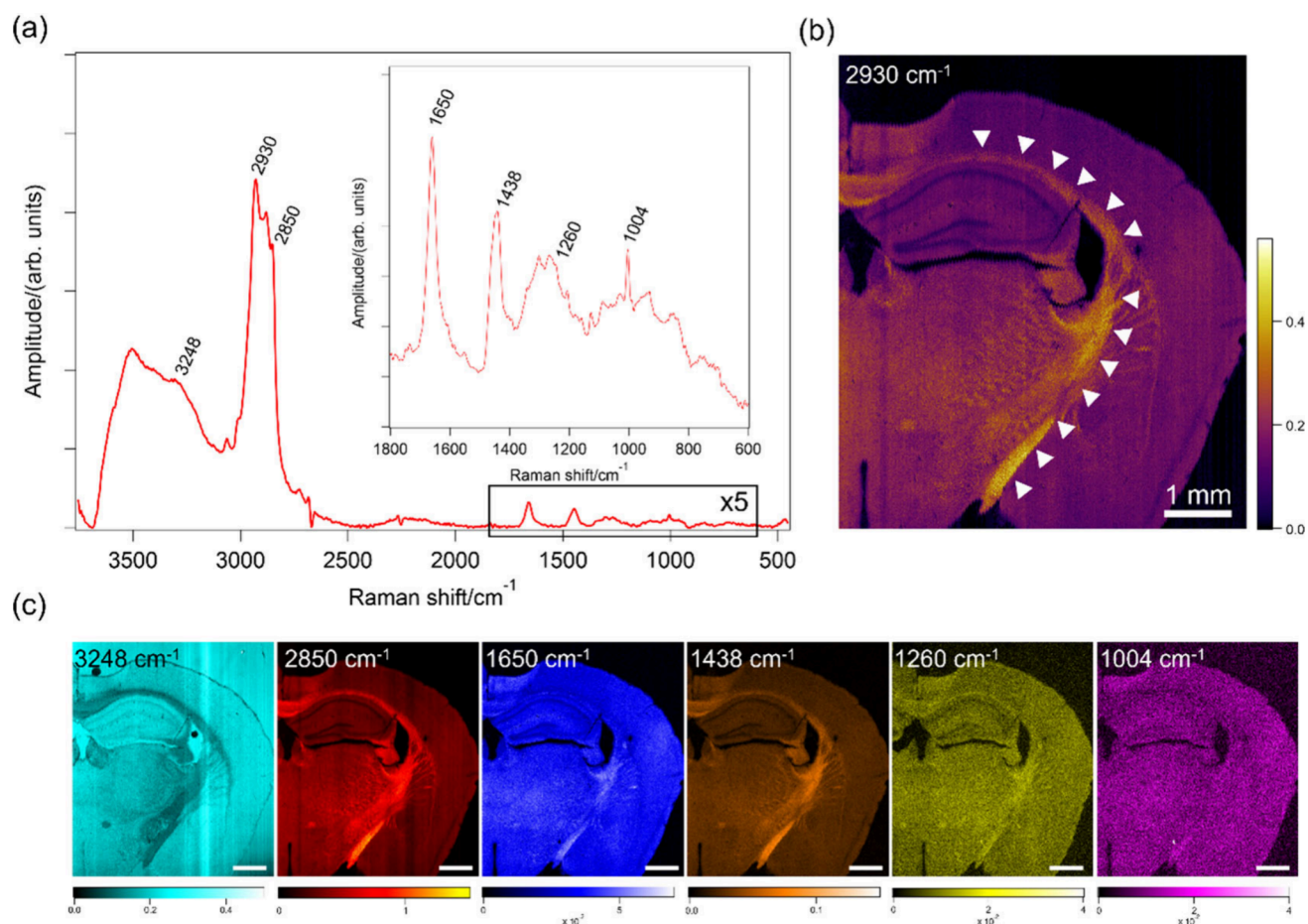
Figure 1. (a) Spectral profile of $\text{Im}[\chi^{(3)}]$ averaged over the brain tissue. The baseline has been subtracted. (b) Images generated using the CARS amplitude at 2930 cm^{-1}. The white triangles indicate regions of white matter. (c) Images generated using the CARS amplitude at 3248, 2850, 1650, 1438, 1260, and 1004 cm^{-1}; each image contains 601 × 631 pixels. The scale bars in panels b and c correspond to 1 mm.

When molecules possess distinctive Raman bands, their identification tends to be straightforward. However, in typical biological tissues, the Raman spectrum in the fingerprint region is often congested, and characteristic Raman bands can be obscured. This scenario also applies to brain tissue, renowned for its diversity of cell phenotypes and biomolecular heterogeneities across distinct regions. Until now, mouse brain slices have been analyzed using CARS[24] and SRS[25,26] microscopies mainly in the C−H stretching region. Beyond the simple classification of lipids and proteins, the visualization of sphingolipids, based on spectral intensities in the C−H stretching region, has been reported.[27] In a subsequent study, SRS imaging of the C = C stretching vibrational mode was demonstrated in the 1550−1750 cm^{-1} spectral region, and hence the distribution of cholesterol was visualized, with the help of deep learning methods.[28] Furthermore, visible preresonance SRS imaging has been used to map the distribution of retinoids, based on the 1550−1750 cm^{-1} spectral region.[29] Studies utilizing CRS microscopy in the fingerprint region have thus far been predominantly focused on specific spectral regions, such as the 1550−1750 cm^{-1} region, as already mentioned, and hence the full potential of the molecular information within vibrational spectra has been overlooked. The combination of spectroscopic imaging across the entire fundamental vibrational range (500−4000 cm^{-1}) with a numerical method to extract physically meaningful information from congested spectra greatly enhances the

molecular specificity of brain microspectroscopy, offering the possibility of revealing as-yet-unknown molecules in the brain.

In this study, we elucidated the molecular fingerprint of brain tissue using ultrabroadband CARS microspectroscopy over the spectral range from 500 to 4000 cm^{-1} with the help of multivariate curve resolution−alternating least-squares (MCR-ALS), revealing as-yet-undiscovered buried Raman bands in the fingerprint region. MCR-ALS was applied to spontaneous Raman imaging in the study performed by Ando et al.[30] Moreover, it was applied to hyperspectral coherent Raman imaging by Zhang et al.[31] and Ragupathy et al.[32] and in our study.[33] In the context of coherent Raman imaging, the spectral region was limited in the CH stretching region, and the data size was limited to 80,[31] 30,[32] and 916[33] spectral points. The present study stands out because the MCR is applied to large data sets of spontaneous-Raman equivalent $\text{Im}[\chi^{(3)}]$ spectra (1248 spectral pixels with 601(x) × 631(y) spatial pixels) both in the CH/OH-stretching and fingerprint regions (500−4000 cm^{-1}). Based on spatio-spectral decomposition using MCR-ALS analysis with such a large data set, we detected spectroscopic signatures attributable to cholesterol and collagen as well as lipids, proteins, water, and nucleic acids in the brain tissue. First, we performed macroscopic measurements of the entire coronal brain sections. Subsequently, we conducted microscopic measurements of the cortex and the brain surface, which are recognized for their distinct heterogeneous molecular distributions. Both the macroscopic
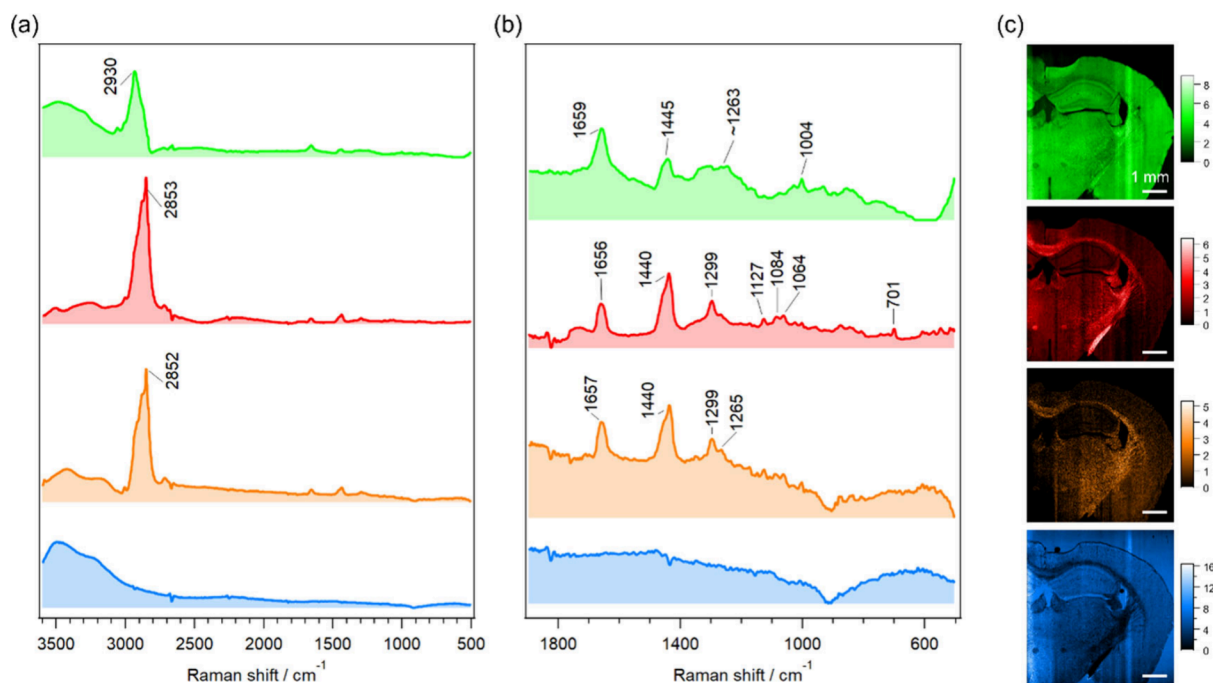
Figure 2. (a) MCR-ALS-decomposed $Im[\chi^{(3)}]$ spectra. (b) Fingerprint region expansion plot and (c) corresponding CARS images. Four physically meaningful components (green, proteins; red, lipid-1; orange, lipid-2; blue, water) were extracted. In the lipid-1 spectral component, a Raman band assigned to cholesterol is visible at 701 cm^{-1}, while the lipid-2 spectral component does not contain the band at 701 cm^{-1}. The scale bar corresponds to 1 mm.

and microscopic measurement results were analyzed by MCR-ALS and examined the molecular fingerprint in each region. Second harmonic generation (SHG) was detected simultaneously with the CARS signal and found to be useful for the visualization of specific organelles in the brain.

■ MATERIALS AND METHODS

A custom-built ultrabroadband multiplex CARS spectroscopic imaging system[23] was modified to allow the imaging of whole mouse brain slices.[34] We used two CARS microspectroscopy systems: one for whole-brain imaging (hereafter referred to as *macroscopic imaging*) and the other for subcellular brain imaging (hereafter referred to as *microscopic imaging*). For the macroscopic imaging acquisitions, the main laser source was a custom-made, dual-fiber, output-synchronized laser source (OPERA: Leukos, Limoges, France). The first laser output, with a wavelength of 1064 nm, temporal duration of 800 ps, and repetition rate of 33 kHz, was used as the pump beam (ω_1) for the CARS process. The second laser output was ultrabroadband supercontinuum radiation, whose NIR spectral components (1100−1800 nm) were used as the Stokes beam (ω_2). These two laser beams were collinearly combined using a notch filter and guided into a modified inverted microscope. The sample was mounted on a motorized stepping stage (MicroDrive: MadCityLabs, Madison, WI, USA) with a scanning range of up to 25 mm in the lateral direction ($x−y$). The laser powers at the sample position were approximately 85 mW for the pump beam and 90 mW for the Stokes beam. The ultrabroadband multiplex CARS signal was detected using a spectrometer (SpectraPro-300i, Princeton Instruments, New Jersey, USA) equipped with a charge coupled device (CCD) camera (PIXIS 100 BR, Princeton Instruments, New Jersey, USA). The spectral range and resolution of the CARS signal were approximately 3500 and 8 cm^{-1}, respectively. The exposure time of the CCD camera for each pixel and total data acquisition time were 100 ms and 10 h, respectively. The prolonged measurement duration (10 h) is principally because of waiting periods for the measurement of each pixel. Therefore, in the future, the measurement duration can be reduced by refining the image acquisition software.

The details of the microscopic imaging setup are described elsewhere.[23] Briefly, the main laser source was a dual-fiber output-synchronized laser with 50−80 ps pulse duration and the repetition rate of 1 MHz (OPERA HP: Leukos, Limoges, France). The setup was similar to that used for the macroscopic imaging; however, the sample was placed on a piezoelectric stage (NANO LP-200: MadCityLabs, Madison, WI, USA) for three-dimensional (xyz) position selection. The full scanning range of the xyz-piezo stage was 200 μm^3. The sample on the piezo stage was raster-scanned (first in the horizontal (x) direction and subsequently in the vertical (y) direction). The laser power at the sample position was approximately 200 mW for the pump beam and 170 mW for the Stokes beam. The exposure time for each pixel was 50 ms for imaging the cortex (Figure 4) and 100 ms for imaging the brain surface (Figure 5). A 100 μm × 100 μm microscopic image of the cortex was obtained; the number of pixels and pixel size were 201 × 201 pixels and 0.5 μm, respectively. A 200 μm × 100 μm image was obtained from the brain surface. The number of pixels and pixel size were 401 × 201 pixels and 0.5 μm, respectively. The setup had multimodal detection capability, allowing the simultaneous collection of a range of light signals from nonlinear optical processes, such as SHG,[35] third harmonic generation (THG), and third-order sum frequency generation (TSFG).[36,37]

Coronal brain slices from wild-type (C57BL/6N) male mice at p90 and p97 were used as samples for the macroscopic and microscopic imaging. Each mouse was deeply anesthetized with 5% isoflurane and intraperitoneally administered with somnopentyl (32.4 mg/kg). Then, the brain was transcardially perfused with 0.1 M phosphate-buffered saline (PBS) containing heparin for 1 min, and then with 4% paraformaldehyde for 10 min. The brain was then removed and immersed in the same fixative buffer (4% paraformaldehyde) at 4 °C for 24 h. Subsequently, the excised brain was rinsed three times with PBS (each rinse involved 5 min of shaking on a shaker) and then sliced to a thickness of 100 μm using a vibratome (VT1000S, Leica Biosystems, Nussloch, Germany). The resulting brain slices were employed for label-free CARS imaging. All the animal experiments were approved by the Institutional Animal Care and Use Committee of the University of Tsukuba. All the animals were maintained in
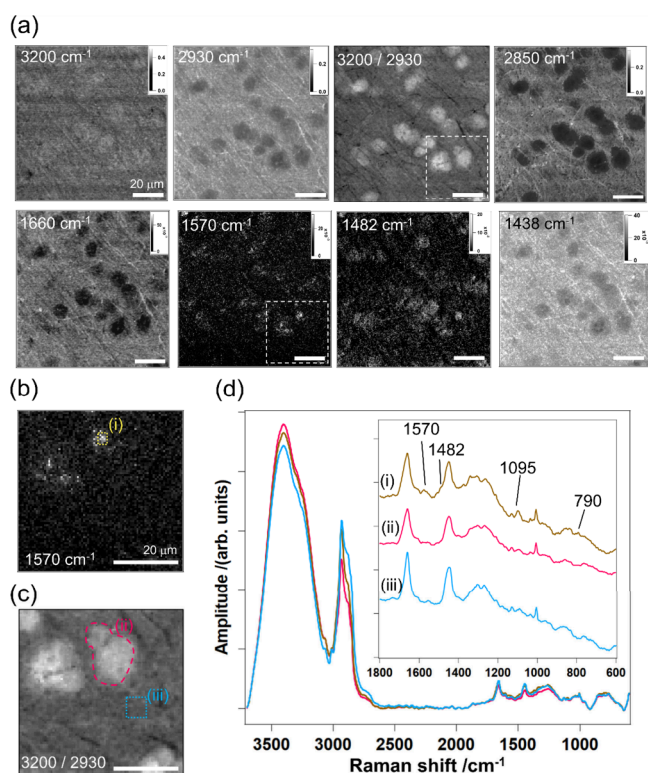
(a)

(b)   (d)

(c)

Figure 3. (a) CARS images of the cortex constructed from the spectral intensities at Raman shifts of 3200, 2930, 2850, 1660, 1570, 1482, and 1438 cm^{-1}, along with an image constructed from the ratio of the spectral intensities at 3200 and 2930 cm^{-1}. The scale bar corresponds to 20 μm. (b) Expanded view of 1570 cm^{-1} CARS image corresponding to the area indicated by the dashed outline in a and c images of the same area constructed using a 3200 cm^{-1}/2930 cm^{-1} intensity ratio as a contrast. (d) Im$[\chi^{(3)}]$ spectra from the areas of the images in b and c indicated by the dashed outline for i, yellow; ii, red; and iii, light blue.

accordance with the institutional guidelines of the animal facilities of the Laboratory of Animal Resource Center.

MCR-ALS was employed to extract the hidden spectroscopic signatures of molecules from the large Raman spectroscopic data set.[30] MCR can be used to decompose measured data, represented as the matrix **A**, using $A \approx \mathbf{WH}$, where the matrix **W** represents the decomposed spectral components, and the matrix **H** contains the intensity profiles corresponding to each decomposed component. Matrix **A** corresponds to the Im$[\chi^{(3)}]$ spectral data set, which has been converted from the raw CARS spectral data set. In this study, as a preprocessing step for the MCR analysis, noise reduction was first performed using singular value decomposition (SVD) on matrix **A**. SVD was applied to the Im$[\chi^{(3)}]$ data set after the MEM retrieval. Subsequently, MCR analysis was carried out using data from the outer regions of the brain tissue, enabling the identification of spectral components corresponding to background and water. Combining these results with the spectra obtained from SVD analysis on matrix A, the number of the initial spectra was determined,[30] and optimization was carried out using ALS. In the ALS optimization, non-negativity constraints for matrices **W** and **H**, l_1-norm regularization (Lasso regression) for matrix **H**, and smoothing constraints for the background spectral components in matrix **W** were imposed, as per a previously reported method.[30] The MCR-ALS calculations were implemented using the Python programming language with the NumPy and SciPy libraries.

RESULTS AND DISCUSSION

We conducted macroscopic imaging to provide an overview of the molecular fingerprint of the brain. The results are shown in Figure 1. More than half of the total area of the mouse brain was visualized in a single image of 6 mm × 6.31 mm in size. Figure 1(a) shows the spectral profile of the Im$[\chi^{(3)}]$ signal averaged over the brain tissue.[38] The Im$[\chi^{(3)}]$ spectrum, equivalent to the spontaneous Raman spectrum, was retrieved from the raw CARS spectrum using MEM.[39] The Raman bands in the fingerprint region are shown in the inset. The Raman shifts of the prominent bands are also shown, as overlaid text, in Figure 1(a). The CARS (Im$[\chi^{(3)}]$) images were reconstructed for slice positions relative to the Bregma of −2 mm. Figures 1(b) and (c) show the outcomes of univariate analysis, in which individual Raman bands were fitted using a Gaussian function to map their amplitudes. The seven CARS images correspond to CH$_3$ stretching (2930 cm^{-1}), OH stretching (3248 cm^{-1}), CH$_2$ stretching (2850 cm^{-1}), Amide I (1650 cm^{-1}), CH$_2$ scissoring (1438 cm^{-1}), = CH bending (1260 cm^{-1}), and phenyl ring breathing (1004 cm^{-1}).

In the CARS image at 2930 cm^{-1} (Figure, 1(b)), white matter, which consists of axons surrounded by a lipid-rich myelin sheath, was clearly visible (indicated by the triangles). The CARS images at 2850, 1438, and 1260 cm^{-1} feature strong signals in the same area. The similarity of these images underscores the fact that ultrabroadband detection is valuable for identifying molecules based on the signals from multiple vibrational resonances associated with the same molecule.

In contrast, the CARS image contrast generated using the signals at 1650 and 1004 cm^{-1}, which originate mainly from proteins, was relatively uniform. Similarly, the CARS image at 3248 cm^{-1}, showing the distribution of water molecules within and surrounding the brain, gives generally low contrast levels across the image. However, the contrast of the CARS image at 3248 cm^{-1} is high within the axon, where the signal associated with lipids is overshadowed by that with water. Thus, we succeeded in decomposing the CARS spectrum into components attributed to lipids, proteins, and water, and reconstructed CARS images to visualize the distributions of these molecules in the brain.

To determine whether there were any hidden Raman bands, we performed multivariate analysis using the MCR-ALS method.[30,33] The results are summarized in Figure 2. Based on the method described in the Materials and Methods section, nine initial spectra were prepared. All nine components are summarized in Figure S1. The MCR-ALS analysis extracts four physically meaningful components (green: proteins, red: lipid 1, orange: lipid 2, blue: water). A distinctive Raman band appeared at 701 cm^{-1} in the lipid-1 component (red plot in Figure 2(b)). Based on previous studies of biomolecules,[28,40−43] this band corresponds to the ring-breathing mode of cholesterol. Therefore, mapping the red component (Figure 2(a)) visualizes cholesterol as well as other lipids. In addition, we identified another lipid component named lipid 2, whose spectral component does not contain the band at 701 cm^{-1}. This component displays relatively prominent Raman bands at 1657 and 1265 cm^{-1}, indicating that the lipid 2 contains relatively high unsaturated lipids. The molecular origin in the present study is unclear and warrants further investigation. Notably, MCR-ALS is effective in removing the smooth baseline overlapped in the CARS (Im$[\chi^{(3)}]$) spectra as shown in components 5−9 in Figure
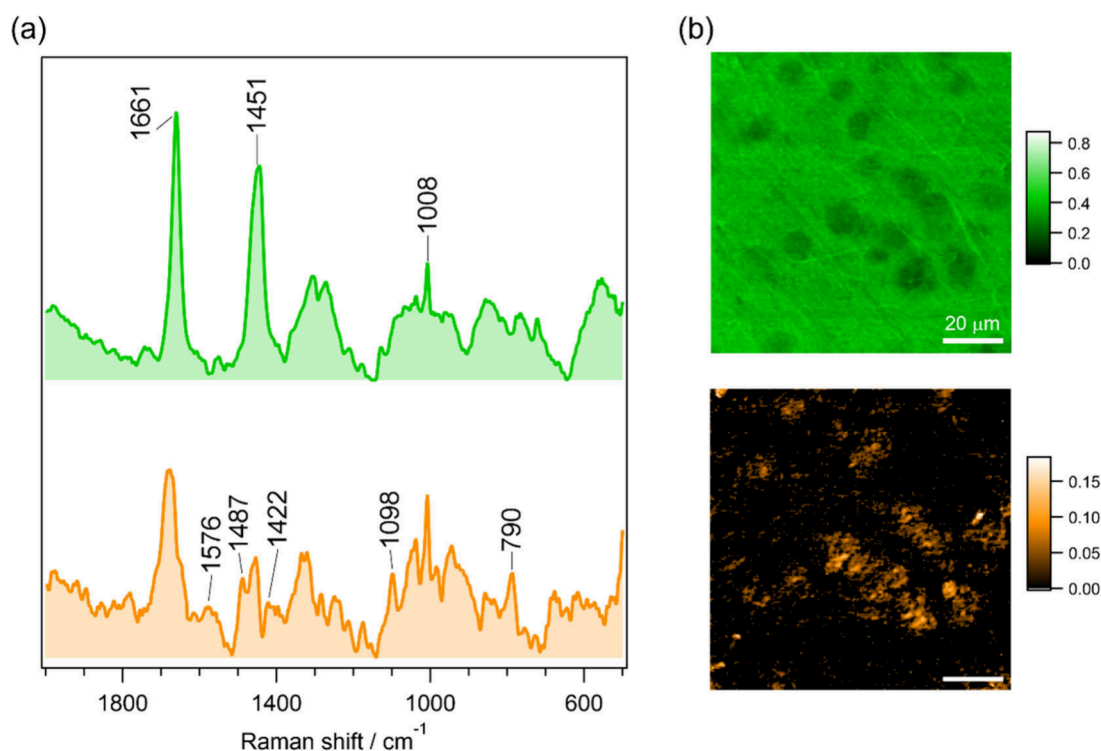
Figure 4. (a) MCR-ALS-decomposed $\text{Im}[\chi^{(3)}]$ spectra in the fingerprint region and (b) corresponding CARS images. Two physically meaningful components (green, proteins; orange, nucleic acids) were extracted. The scale bars in panel b correspond to 20 μm.

S1. A similar strategy was employed to remove autofluorescence in spontaneous Raman spectroscopy.[30]

In this section, we quantitatively discuss the need for MCR-ALS in our study by evaluating the signal-to-noise ratio (SNR). Following the criterion for the signal detection limit as defined by Parekh et al.,[17] where SNR $\approx$ 1, we calculated the spatially averaged $\text{Im}[\chi^{(3)}]$ spectra for the Raman band at 701 cm^{-1}. We compared the spectral noise levels with the signal amplitude, and determined the spatially averaged pixel size that results in SNR > 1 (Figure S2). Consequently, the amplitude of the band at 701 cm^{-1} was below the detection limit with SNR < 1 for a single pixel, requiring an average of 5 pixels to achieve SNR > 1. Therefore, MCR-ALS is necessary, particularly for weak Raman bands such as the band at 701 cm^{-1}. The combination of ultrabroadband CARS detection aided with MCR-ALS is effective in uncovering hidden Raman bands, reducing the potential risk of overlooking small Raman bands.

To investigate the molecular distribution at different positions, we conducted CARS imaging on a series of brain slices obtained from various locations relative to the Bregma. Figure S3 shows a series of images constructed using the CARS signals at 2930 (proteins/lipids), 2850 (lipids), 1660 (proteins/lipids), and 1438 (lipids) cm^{-1}, as representative images showing proteins and lipids distributions.

To explore the molecular fingerprints of biomolecules other than lipids, proteins, water, and cholesterol, we conducted microscopic CARS imaging. As representative areas with distinct cell heterogeneity and biomolecular diversity, we first focused on the cortex. The cortex, which consists of cortical tissue, is the outermost layer of the brain. The cortex is composed of a layer of neurons arranged in laminae. Figure 3(a) shows images constructed using the CARS signal at 3200, 2930, 2850, 1660, 1570, 1482, and 1438 cm^{-1}. Round dark areas, indicated by the red dashed outline (ii), with diameters

of approximately 10 μm are observed in the 2930, 2850, and 1660 cm^{-1} CARS images. Our previous research showed that the protein and lipid concentrations in the nucleus are lower than those in the cytoplasm.[19,20] Therefore, these round dark areas correspond to the nuclei of cells, such as neurons and glial cells, in the cortex. Upon examining the 3200 cm^{-1} image in Figure 3(a), the water concentration appears to be slightly higher in the nucleus with respect to that in the other regions. Given that the protein and lipid concentrations in the nucleus are low, this observation prompted us to conduct the following analysis. Using the ratio between the spectral intensities at 3200 and 2930 cm^{-1} as a contrast, we constructed the ratio image in Figure 3(a), in which the cell nuclei are significantly enhanced. Thus, the concentration of proteins and lipids in the cell nucleus is significantly lower than in other cellular areas.

Furthermore, we observed strong signals within the areas corresponding to the nuclei in the CARS images at 1570 and 1482 cm^{-1}, indicated by the yellow dashed outline (i). These Raman bands are assigned to purine-ring breathing bands of adenine and guanine in RNA and DNA. As these bands provide particularly strong signals from the nucleoli within the cell nuclei,[19,20] we concluded that the CARS signals at 1570 and 1482 cm^{-1} could be assigned primarily to the nucleoli; hence, the images constructed using the intensities at these Raman shifts as contrasts can be interpreted as visualizations of nucleoli. Expanded views of the CARS images are presented in Figures 3(b) and (c). The 1570 cm^{-1} CARS image has strong signals within the nuclei, which are most apparent in the image constructed using the 3200 cm^{-1}/2930 cm^{-1} CARS intensity ratio as contrast. The $\text{Im}[\chi^{(3)}]$ spectra in the three areas indicated in Figures 3(b) and (c) are shown in Figure 3(d). Small yet distinctive Raman bands are observed at 1570 and 1482 cm^{-1}, which were used for reconstructing the aforementioned CARS images. These spectral features are
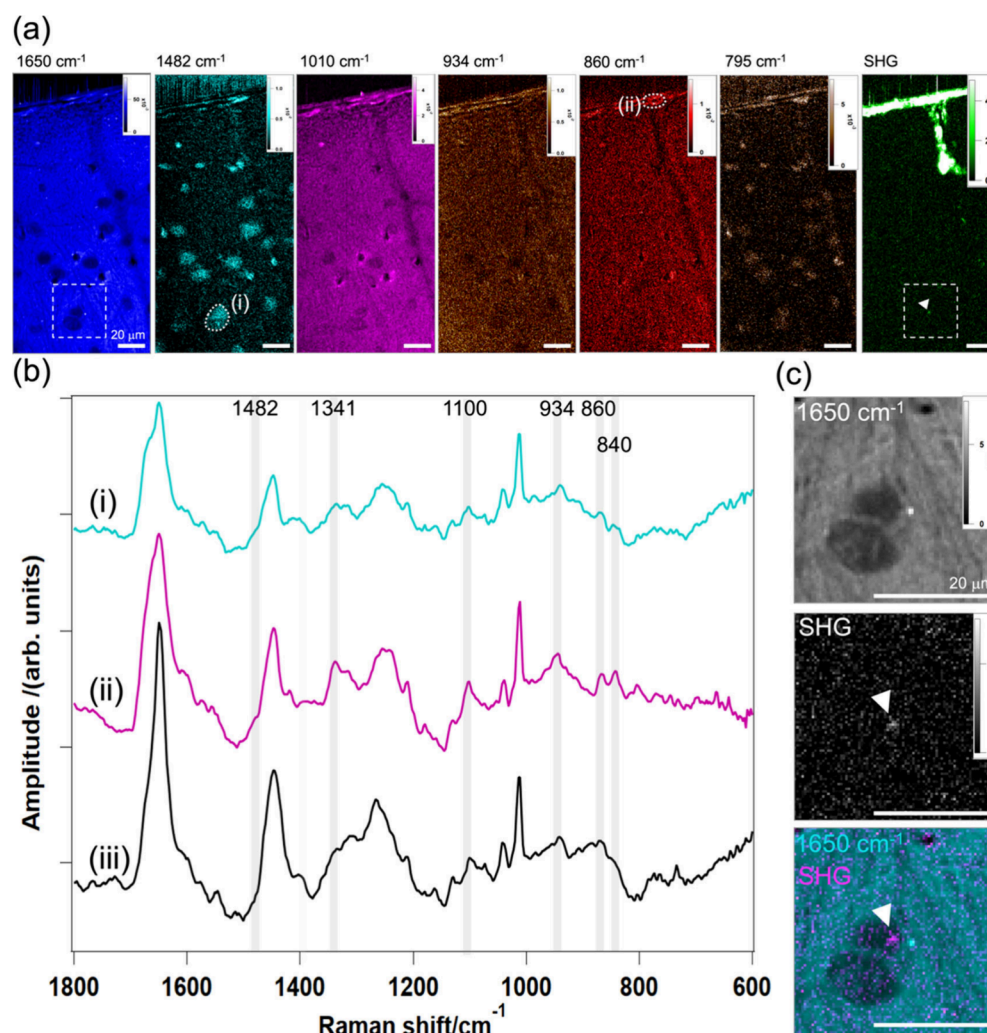
Figure 5. (a) CARS images of the brain surface constructed from the intensities of the Raman shifts at 1650, 1482, 1010, 934, 866, and 795 cm^{-1}. An SHG image of the same area is also shown. (b) Spectral profiles of Im[$\chi^{(3)}$] in the two areas indicated in a (i and ii) and averaged over the entire area of the imaged tissue (iii). (c) Expanded views of the CARS image at 1650 cm^{-1}, SHG, and merged SHG−CARS images. The scale bar corresponds to 20 μm.

not present in the cytoplasm, as indicated by the light-blue dashed outline (iii).

The same area was also examined using the MCR-ALS. The results are shown in Figure 4. Based on the method described in the Materials and Methods section, eight initial spectra were prepared (Figure S4). Here we focused on the fingerprint region. The two physically meaningful components (shown as green and orange plots in Figure 4(a)) were respectively assigned to proteins and nucleic acids. As mentioned in the discussion of the univariate analysis (illustrated in Figure 3), round dark areas with diameters of approximately 10 μm can be seen in the image in Figure 4(b) corresponding to proteins (green). The orange component represents multiple Raman bands assigned to nucleic acids, at 1576, 1487, 1422, 1098, and 790 cm^{-1}, and hence this component allows effective visualization of nuclei in the cellular nuclei. MCR-ALS has proven effective in detecting multiple weak bands that were not apparent in the univariate analysis. Thus, we successfully extracted spectroscopic features on nucleic acids and visualized the nuclear structures within the cortex.

Benefiting from our previous explorations,[44] the second focus of this study was the brain surface, with the aim of

elucidating the molecular fingerprint of collagen in the arachnoid membrane and blood vessels. Figure 5 shows CARS microspectroscopic images and analysis of the brain surface. Figure 5(a) shows the CARS images obtained at 1650, 1482, 1010, 934, 860, and 795 cm^{-1}. Similar to our observation in our cortex imaging study, the 1650 cm^{-1} CARS image of the brain surface features round dark areas, possibly corresponding to cell nuclei. We observed that these areas are strongly correlated with the bright round areas seen in the 1482 and 795 cm^{-1} CARS images. Based on our previous findings,[19] the Raman band at 795 cm^{-1} originates from the pyrimidine rings of thymine, cytosine, and uracil in DNA/RNA. The CARS signals at both 1482 and 795 cm^{-1} are distributed in regions with sizes corresponding to cell nuclei, suggesting that these bands can be used to visualize nuclei. The similarity between these CARS images is further evidence to support the aforementioned assignment. By contrast, the CARS image at 1010 cm^{-1} maps the phenylalanine residues within proteins, and hence a quite consistently uniform signal, with little contrast between different areas, was seen across the tissue.

We observed pronounced contrast in the SHG image of the brain surface (Figure 5(a)), in agreement with our previous
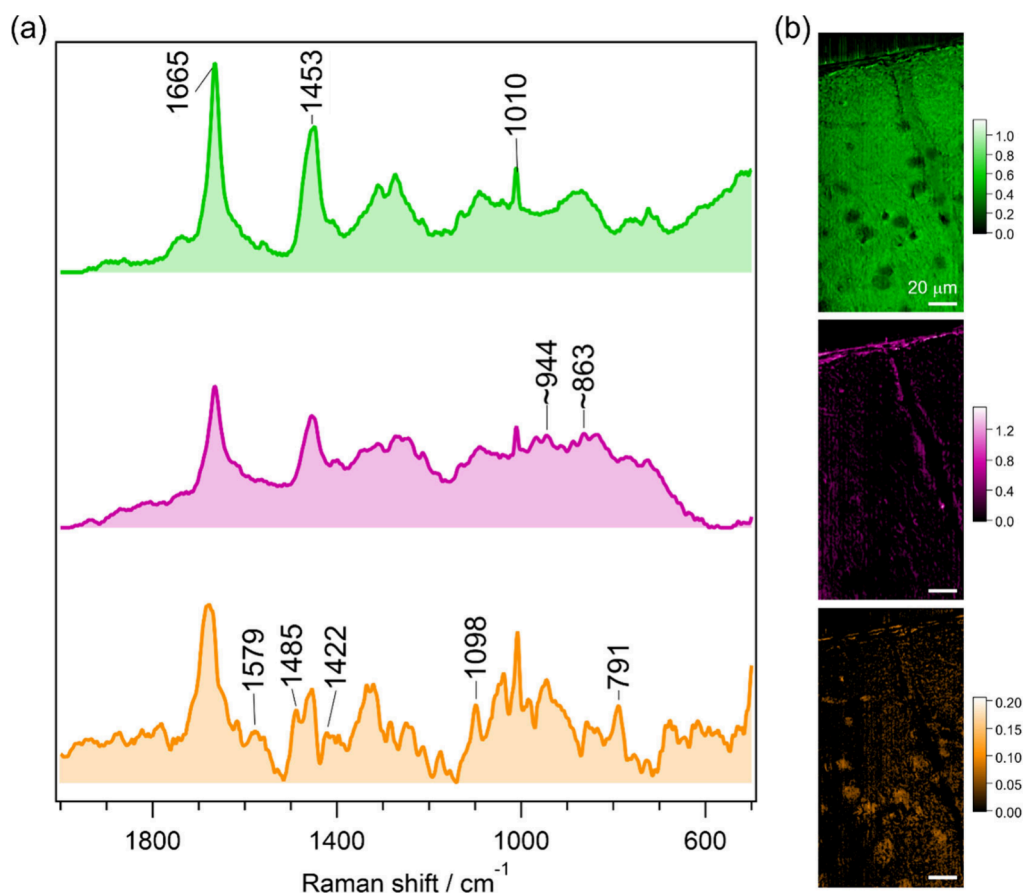
Figure 6. (a) MCR-ALS-decomposed $\mathrm{Im}[\chi^{(3)}]$ spectra in the fingerprint region and (b) corresponding CARS images. Three physically meaningful components (green, proteins; purple, collagen; and orange, nucleic acids) were extracted. The scale bars in panel b correspond to 1 mm.

findings.[44] In that study, we attributed the SHG signal observed on the brain surface to the collagen content of the arachnoid membrane. The consistent visibility of the SHG signal in similar areas in the present study supports our conclusion that the collagen distribution in the arachnoid membrane was visualized in the map of the SHG signal. In the present study, further confirmation was obtained using the molecular fingerprint in the $\mathrm{Im}[\chi^{(3)}]$ spectrum. According to the literature,[18,45,46] collagen exhibits two characteristic Raman bands at approximately 857 and 938 cm^{-1}. The spatially averaged $\mathrm{Im}[\chi^{(3)}]$ spectrum in the region with strong SHG signal is shown in Figure 5(b) (spectrum (ii)), where the molecular fingerprint of collagen confirms its presence. This feature around 850−950 cm^{-1} is not observed in the spectral profile of (iii), corresponding to the spatial average over the entire area of the imaged tissue.

Upon careful examination of the SHG images, we also identified other areas with pronounced contrast. First, the tubular structure extending from the arachnoid membrane was identified as a blood vessel based on its morphology. Second, weak but distinct spots of SHG signal were observed at the areas indicated by three triangles. One of the areas is enlarged in Figure 5(c), which shows a CARS image at 1650 cm^{-1} (top), SHG image (middle), and their merged image (bottom). As indicated in the merged image, the weak SHG spot is observed around the cell nucleus. Based on our previous studies of retinal photoreceptors[35] and human embryonic kidney cells,[44] we conclude that these spots are Rootletin filaments such as ciliary rootlet.[35] Intriguingly, in Figure 5(c),

the CARS image at 1650 cm^{-1} also features a bright spot near the nucleus. Upon examining the merged SHG−CARS image, the bright spot observed in the CARS image at 1650 cm^{-1} was spatially distinct from that observed in the SHG image. Presumably, the structure visualized in the CARS image at 1650 cm^{-1} was a lipid-rich particle, whereas that observed in the SHG image corresponds to Rootletin filaments. Thus, aided by SHG, we identified the molecular fingerprint of collagen in the arachnoid membrane. While the Rootletin filament was visualized using SHG, it was difficult to identify its molecular fingerprint by CARS, probably due to low concentration.

The same image area was also examined using MCR-ALS. Based on the method described in the Materials and Methods section, ten initial spectra were prepared (Figure S5). The results (Figure 6) show that three physically meaningful components were extracted (green: proteins, purple: collagen, orange: nucleic acids). Similar to our observations based on the univariate analysis (Figure 5), round dark areas in the image of the green component correspond to nuclei. The purple component includes the Raman bands at ∼994 and ∼863 cm^{-1} that are assigned to collagen, and hence this component allows effective visualization of the arachnoid membrane and a blood vessel. A similar assignment was previously reported.[6] The orange component includes characteristic bands corresponding to nucleic acids at 1579, 1485, 1422, 1098, and 791 cm^{-1}, and hence this component visualizes nuclei. Thus, we successfully extracted spectroscopic markers of collagen and nucleic acids, and visualized the

arachnoid membrane, a blood vessel, and nuclei within the cortex.

CONCLUSION

In summary, we developed a method for the multivariate analysis of the entire fundamental vibrational region of ultrabroadband multiplex CARS microspectroscopic image based on MCR-ALS analysis. We successfully identified the molecular signatures of lipids, proteins, and water, as well as those of cholesterol, collagen, and nucleic acids within brain tissue This approach underscores the utility of molecular fingerprinting. Although our investigation primarily focused on established Raman bands, our results suggest the potential to discern unique spectral patterns indicative of brain dysfunction within the fingerprint region by comparing healthy and diseased brains. Given that the molecular fingerprints of biological molecules are largely preserved across species, this methodology can serve as an invaluable tool for label-free imaging across various disciplines in the life sciences.

ASSOCIATED CONTENT

Ⓢ Supporting Information

The Supporting Information is available free of charge at https://pubs.acs.org/doi/10.1021/cbmi.4c00034.

> Figure S1 shows the MCR decomposition of macroscopic measurement. Figure S2 shows the comparison of MCR-ALS and the univariate analysis at the 701 cm^{-1} band. Figure S3 shows series of CARS images at 2930, 2850, 1660, and 1438 cm^{-1} of brain slices from different positions relative to the bregma. Figure S4 shows MCR decomposition of microscopic measurement at the cortex. Figure S5 shows MCR decomposition of microscopic measurement at the brain surface (PDF)

AUTHOR INFORMATION

Corresponding Author

Hideaki Kano − *Department of Chemistry, Faculty of Science, Kyushu University, Fukuoka 819-0395, Japan*; Present Address: Department of Biosciences and Informatics Faculty of Science and Technology, Keio University 3-14-1 Hiyoshi, Kohoku-ku, Yokohama, Kanagawa 223-8522, Japan; ⓞ orcid.org/0000-0003-3682-7627; Email: hkano@chem.kyushu-univ.jp, hkano@bio.keio.ac.jp

Authors

Yusuke Murakami − *Ph.D. Program in Humanics, University of Tsukuba, Tsukuba, Ibaraki 305-8577, Japan; International Institute for Integrative Sleep Medicine (WPI-IIIS), Tsukuba, Ibaraki 305-8575, Japan*

Masahiro Ando − *Research Organization for Nano and Life Innovation, Waseda University, Tokyo 162-0041, Japan*

Ayako Imamura − *Ph.D. Program in Humanics, University of Tsukuba, Tsukuba, Ibaraki 305-8577, Japan; International Institute for Integrative Sleep Medicine (WPI-IIIS), Tsukuba, Ibaraki 305-8575, Japan*

Ryosuke Oketani − *Department of Chemistry, Faculty of Science, Kyushu University, Fukuoka 819-0395, Japan*

Philippe Leproux − *Institut de Recherche XLIM, UMR CNRS No. 7252, 87060 Limoges CEDEX, France*

Sakiko Honjoh − *International Institute for Integrative Sleep Medicine (WPI-IIIS), Tsukuba, Ibaraki 305-8575, Japan*

Complete contact information is available at:
https://pubs.acs.org/10.1021/cbmi.4c00034

Notes

The authors declare no competing financial interest.

REFERENCES

(1) Day, J. P. R.; Domke, K. F.; Rago, G.; Kano, H.; Hamaguchi, H.; Vartiainen, E. M.; Bonn, M. Quantitative Coherent Anti-Stokes Raman Scattering (CARS) Microscopy. *J. Phys. Chem. B* **2011**, *115* (24), 7713−7725.

(2) Evans, C. L.; Xie, X. S. Coherent Anti-Stokes Raman Scattering Microscopy: Chemical Imaging for Biology and Medicine. *Annu. Rev. Anal. Chem.* **2008**, *1*, 883−909.

(3) Kano, H. Molecular Spectroscopic Imaging Using a White-Light Laser Source. *Bull. Chem. Soc. Jpn.* **2010**, *83* (7), 735−743.

(4) Min, W.; Freudiger, C. W.; Lu, S. J.; Xie, X. S. Coherent Nonlinear Optical Imaging: Beyond Fluorescence Microscopy. *Annu. Rev. Phys. Chem.* **2011**, *62*, 507−530.

(5) Chung, C.-Y.; Potma, E. O. Biomolecular Imaging with Coherent Nonlinear Vibrational Microscopy. *Annu. Rev. Phys. Chem.* **2013**, *64*, 77−99.

(6) Camp, C. H.; Cicerone, M. T. Chemically sensitive bioimaging with coherent Raman scattering. *Nat. Photonics* **2015**, *9* (5), 295−305.

(7) Zhang, C.; Zhang, D. L.; Cheng, J. X. Coherent Raman Scattering Microscopy in Biology and Medicine. In *Annual Review of Biomedical Engineering*; Yarmush, M. L., Ed.; Annual Review of Biomedical Engineering; 2015; Vol. 17, pp 415−445.

(8) Yue, S.; Cheng, J.-X. Deciphering single cell metabolism by coherent Raman scattering microscopy. *Curr. Opin. Chem. Biol.* **2016**, *33*, 46−57.

(9) Kano, H.; Segawa, H.; Okuno, M.; Leproux, P.; Couderc, V. Hyperspectral coherent Raman imaging - principle, theory, instrumentation, and applications to life sciences. *J. Raman Spectrosc.* **2016**, *47* (1), 116−123.

(10) Cicerone, M. Molecular imaging with CARS micro-spectroscopy. *Curr. Opin. Chem. Biol.* **2016**, *33*, 179−185.

(11) Astratov, V. N.; Sahel, Y. B.; Eldar, Y. C.; Huang, L.; Ozcan, A.; Zheludev, N.; Zhao, J.; Burns, Z.; Liu, Z.; Narimanov, E.; et al. Roadmap on Label-Free Super-Resolution Imaging. *Laser Photonics Rev.* **2023**, *17* (12), 2200029.

(12) Masia, F.; Glen, A.; Stephens, P.; Borri, P.; Langbein, W. Quantitative Chemical Imaging and Unsupervised Analysis Using Hyperspectral Coherent Anti-Stokes Raman Scattering Microscopy. *Anal. Chem.* **2013**, *85* (22), 10820−10828.

(13) Camp, C. H., Jr; Bender, J. S.; Lee, Y. J. Real-time and high-throughput Raman signal extraction and processing in CARS hyperspectral imaging. *Opt. Express* **2020**, *28* (14), 20422−20437.

(14) Kee, T. W.; Cicerone, M. T. Simple approach to one-laser, broadband coherent anti-Stokes Raman scattering microscopy. *Opt. Lett.* **2004**, *29* (23), 2701–2703.

(15) Kano, H.; Hamaguchi, H. Ultrabroadband (> 2500 cm(−1)) multiplex coherent anti-Stokes Raman scattering microspectroscopy using a supercontinuum generated from a photonic crystal fiber. *Appl. Phys. Lett.* **2005**, *86* (12), 121113.

(16) Okuno, M.; Kano, H.; Leproux, P.; Couderc, V.; Day, J. P. R.; Bonn, M.; Hamaguchi, H. Quantitative CARS Molecular Fingerprinting of Single Living Cells with the Use of the Maximum Entropy Method. *Angew. Chem., Int. Ed.* **2010**, *49* (38), 6773–6777.

(17) Parekh, S. H.; Lee, Y. J.; Aamer, K. A.; Cicerone, M. T. Label-Free Cellular Imaging by Broadband Coherent Anti-Stokes Raman Scattering Microscopy. *Biophys. J.* **2010**, *99* (8), 2695–2704.

(18) Camp, C. H., Jr; Cicerone, M. T. Chemically sensitive bioimaging with coherent Raman scattering. *Nat. Photonics* **2015**, *9* (5), 295–305.

(19) Yoneyama, H.; Sudo, K.; Leproux, P.; Couderc, V.; Inoko, A.; Kano, H. CARS molecular fingerprinting using sub-100-ps microchip laser source with fiber amplifier. *APL Photonics* **2018**, *3* (9), 092408.

(20) Kano, H.; Maruyama, T.; Kano, J.; Oka, Y.; Kaneta, D.; Guerenne, T.; Leproux, P.; Couderc, V.; Noguchi, M. Ultra-multiplex CARS spectroscopic imaging with 1-ms pixel dwell time. *OSA Continuum* **2019**, *2* (5), 1693–1705.

(21) Ishitsuka, K.; Koide, M.; Yoshida, M.; Segawa, H.; Leproux, P.; Couderc, V.; Watanabe, M. M.; Kano, H. Identification of intracellular squalene in living algae, Aurantiochytrium mangrovei with hyperspectral coherent anti-Stokes Raman microscopy using a sub-nanosecond supercontinuum laser source. *J. Raman Spectrosc.* **2017**, *48*, 8–15.

(22) Oka, Y.; Yoshida, M.; Minoda, A.; Leproux, P.; Watanabe, M. M.; Kano, H. Label-free detection of polysulfides and glycogen of Cyanidium caldarium using ultra-multiplex coherent anti-Stokes Raman scattering microspectroscopy. *J. Raman Spectrosc.* **2021**, *52* (12), 2572–2580.

(23) Tanaka, K.; Oketani, R.; Terada, T.; Leproux, P.; Morono, Y.; Kano, H. Label-Free Identification of Spore-Forming Bacteria Using Ultrabroadband Multiplex Coherent Anti-Stokes Raman Scattering Microspectroscopy. *J. Phys. Chem. B* **2023**, *127* (9), 1940–1946.

(24) Evans, C. L.; Xu, X. Y.; Kesari, S.; Xie, X. S.; Wong, S. T. C.; Young, G. S. Chemically-selective imaging of brain structures with CARS microscopy. *Opt. Express* **2007**, *15* (19), 12076–12087.

(25) Ji, M. B.; Orringer, D. A.; Freudiger, C. W.; Ramkissoon, S.; Liu, X. H.; Lau, D.; Golby, A. J.; Norton, I.; Hayashi, M.; Agar, N. Y. R. Rapid, Label-Free Detection of Brain Tumors with Stimulated Raman Scattering Microscopy. *Science Translational Medicine* **2013**, *5* (201), 201ra119.

(26) He, R.; Xu, Y.; Zhang, L.; Ma, S.; Wang, X.; Ye, D.; Ji, M. Dual-phase stimulated Raman scattering microscopy for real-time two-color imaging. *Optica* **2017**, *4* (1), 44.

(27) Bi, Y.; Yang, C.; Chen, Y.; Yan, S.; Yang, G.; Wu, Y.; Zhang, G.; Wang, P. Near-resonance enhanced label-free stimulated Raman scattering microscopy with spatial resolution near 130 nm. *Light-Sci. Appl.* **2018**, *7* (1), 81.

(28) Lin, H.; Lee, H. J.; Tague, N.; Lugagne, J. B.; Zong, C.; Deng, F.; Shin, J.; Tian, L.; Wong, W.; Dunlop, M. J.; Cheng, J. X. Microsecond fingerprint stimulated Raman spectroscopic imaging by ultrafast tuning and spatial-spectral learning. *Nat. Commun.* **2021**, *12* (1), 3052.

(29) Zhuge, M.; Huang, K. C.; Lee, H. J.; Jiang, Y.; Tan, Y.; Lin, H.; Dong, P. T.; Zhao, G.; Matei, D.; Yang, Q.; Cheng, J. X. Ultrasensitive Vibrational Imaging of Retinoids by Visible Preresonance Stimulated Raman Scattering Microscopy. *Advanced science* **2021**, *8* (9), 2003136.

(30) Ando, M.; Hamaguchi, H. Molecular component distribution imaging of living cells by multivariate curve resolution analysis of space-resolved Raman spectra. *Journal of biomedical optics* **2014**, *19* (1), 011016.

(31) Zhang, D.; Wang, P.; Slipchenko, M. N.; Ben-Amotz, D.; Weiner, A. M.; Cheng, J.-X. Quantitative Vibrational Imaging by Hyperspectral Stimulated Raman Scattering Microscopy and Multivariate Curve Resolution Analysis. *Anal. Chem.* **2013**, *85* (1), 98–106.

(32) Chitra Ragupathy, I.; Schweikhard, V.; Zumbusch, A. Multivariate analysis of hyperspectral stimulated Raman scattering microscopy images. *J. Raman Spectrosc.* **2021**, *52* (9), 1630–1642 (acccessed 2024/05/20).

(33) Boildieu, D.; Guerenne-Del Ben, T.; Duponchel, L.; Sol, V.; Petit, J.-M.; Champion, É.; Kano, H.; Helbert, D.; Magnaudeix, A.; Leproux, P.; Carré, P. Coherent anti-Stokes Raman scattering cell imaging and segmentation with unsupervised data analysis. *Frontiers in Cell and Developmental Biology* **2022**, *10*, DOI: 10.3389/fcell.2022.933897.

(34) Murakami, Y.; Miyazaki, S.; Boildieu, D.; Rajaofara, Z.; Helbert, D.; Magnaudeix, A.; Carré, P.; Leproux, P.; Honjoh, S.; Hideaki, K. Toward whole brain label-free molecular imaging with single-cell resolution sing ultra-broadband multiplex CARS microspectroscopy. *Proc. SPIE* **2022**, PC119731B.

(35) Akiyama, T.; Inoko, A.; Kaji, Y.; Yonemura, S.; Kakiguchi, K.; Segawa, H.; Ishitsuka, K.; Yoshida, M.; Numata, O.; Leproux, P.; et al. SHG-specificity of cellular Rootletin filaments enables naive imaging with universal conservation. *Sci. Rep.* **2017**, *7*, 39967.

(36) Segawa, H.; Okuno, M.; Kano, H.; Leproux, P.; Couderc, V.; Hamaguchi, H. Label-free tetra-modal molecular imaging of living cells with CARS, SHG, THG and TSFG (coherent anti-Stokes Raman scattering, second harmonic generation, third harmonic generation and third-order sum frequency generation). *Opt. Express* **2012**, *20* (9), 9551–9557.

(37) Segawa, H.; Fukutake, N.; Leproux, P.; Couderc, V.; Ozawa, T.; Kano, H. Electronically resonant third-order sum frequency generation spectroscopy using a nanosecond white-light supercontinuum. *Opt Express* **2014**, *22* (9), 10416–10429.

(38) Murakami, Y.; Oketani, R.; Leproux, P.; Nuriya, M.; Honjoh, S.; Hideaki, K. *Molecular Identification of Second Harmonic Generation (SHG) Sources in Mouse Brain by Multimodal Imaging with Ultra-Broadband Multiplex Coherent Anti Stokes Raman Scattering (CARS)*; SPIE, 2024.

(39) Vartiainen, E. M.; Rinia, H. A.; Müller, M.; Bonn, M. Direct extraction of Raman line-shapes from congested CARS spectra. *Opt. Express* **2006**, *14*, 3622–3630.

(40) Krafft, C.; Neudert, L.; Simat, T.; Salzer, R. Near infrared Raman spectra of human brain lipids. *Spectrochim. Acta, Part A* **2005**, *61* (7), 1529–1535.

(41) Lee, S. S.-Y.; Li, J.; Tai, J. N.; Ratliff, T. L.; Park, K.; Cheng, J.-X. Avasimibe Encapsulated in Human Serum Albumin Blocks Cholesterol Esterification for Selective Cancer Treatment. *ACS Nano* **2015**, *9* (3), 2420–2432.

(42) Autefage, H.; Gentleman, E.; Littmann, E.; Hedegaard, M. A. B.; Von Erlach, T.; O'Donnell, M.; Burden, F. R.; Winkler, D. A.; Stevens, M. M. Sparse feature selection methods identify unexpected global cellular response to strontium-containing materials. *Proc. Natl. Acad. Sci. U. S. A.* **2015**, *112* (14), 4280–4285.

(43) Wang, N.; Wang, J.; Wang, P.; Ji, N.; Yue, S. Label-Free Raman Spectromicroscopy Unravels the Relationship between MGMT Methylation and Intracellular Lipid Accumulation in Glioblastoma. *Anal. Chem.* **2023**, *95* (31), 11567–11571.

(44) Murakami, Y.; Masaki, M.; Miyazaki, S.; Oketani, R.; Hayashi, Y.; Yanagisawa, M.; Honjoh, S.; Kano, H. Spectroscopic second and third harmonic generation microscopy using a femtosecond laser source in the third near-infrared (NIR-III) optical window. *Biomed. Opt. Express* **2022**, *13* (2), 694–708.

(45) Frushour, B. G.; Koenig, J. L. Raman scattering of collagen, gelatin, and elastin. *Biopolymers* **1975**, *14* (2), 379–391.

(46) Villaret, A.; Ipinazar, C.; Satar, T.; Gravier, E.; Mias, C.; Questel, E.; Schmitt, A.-M.; Samouillan, V.; Nadal, F.; Josse, G. Raman characterization of human skin aging. *Skin Res. Technol.* **2019**, *25* (3), 270–276.